Towards Eddy-Resolving Models of the Arctic Ocean

Wieslaw Maslowski and Jaclyn Clement Kinney

Department of Oceanography, Naval Postgraduate School, Monterey, California, USA

Douglas C. Marble

Office of Naval Research, Code 322, Arlington, Virginia, USA

Jaromir Jakacki

Institute of Oceanology, Polish Academy of Sciences, Sopot, Poland

High-resolution model results from two regional grid configurations, 1/6° and 1/12°, for the pan-Arctic domain are intercompared and validated against limited observational data to examine the main characteristics and distribution of simulated eddies and to determine limitations of the employed spatial resolution. Several regions within the larger domain are examined in particular: the Gulf of Alaska, Bering Sea, Chukchi Sea, Labrador Sea, Nordic Seas, and Barents Sea. These regions are selected either because of their known high-level eddy activity and/or because some data exist there for model validation. We find that doubling horizontal resolution roughly from 18 km to 9 km increases mean eddy kinetic energy (EKE) by an order of magnitude or more. In some regions, such as the southern Labrador Sea and the Gulf of Alaska, EKE distribution from the 1/12° model compares well, both in magnitude and spatial distribution, with estimates from observations. Model and altimeter estimates of EKE in the sub-Arctic Pacific both show high values associated with the Alaskan Stream and low values in the western Gulf of Alaska and deep Bering Sea. The model EKE values are less than the altimeter EKE values along the shelf break in the central Bering Sea. Spectral analysis of model and altimeter-measured sea surface topography suggest that the 9-km grid is not sufficient to fully resolve eddy features with wavelengths shorter than 100–150 km. Presented regional analyses imply that spatial resolution of order few kilometers is needed to fully represent eddy energetics in the Arctic Ocean.

1. INTRODUCTION

The primary focus of this chapter is to analyze the simulated eddy kinetic energy (EKE) in increasingly high-resolution model configurations of the pan-Arctic region and to illustrate the gains realized from doubling model resolution from 18 km to 9 km. The comparison is between two regional coupled ice ocean models with many similar characteristics (Figure 1, Table 1).

Ocean Modeling in an Eddying Regime
Geophysical Monograph Series 177

10.1029/177GM16

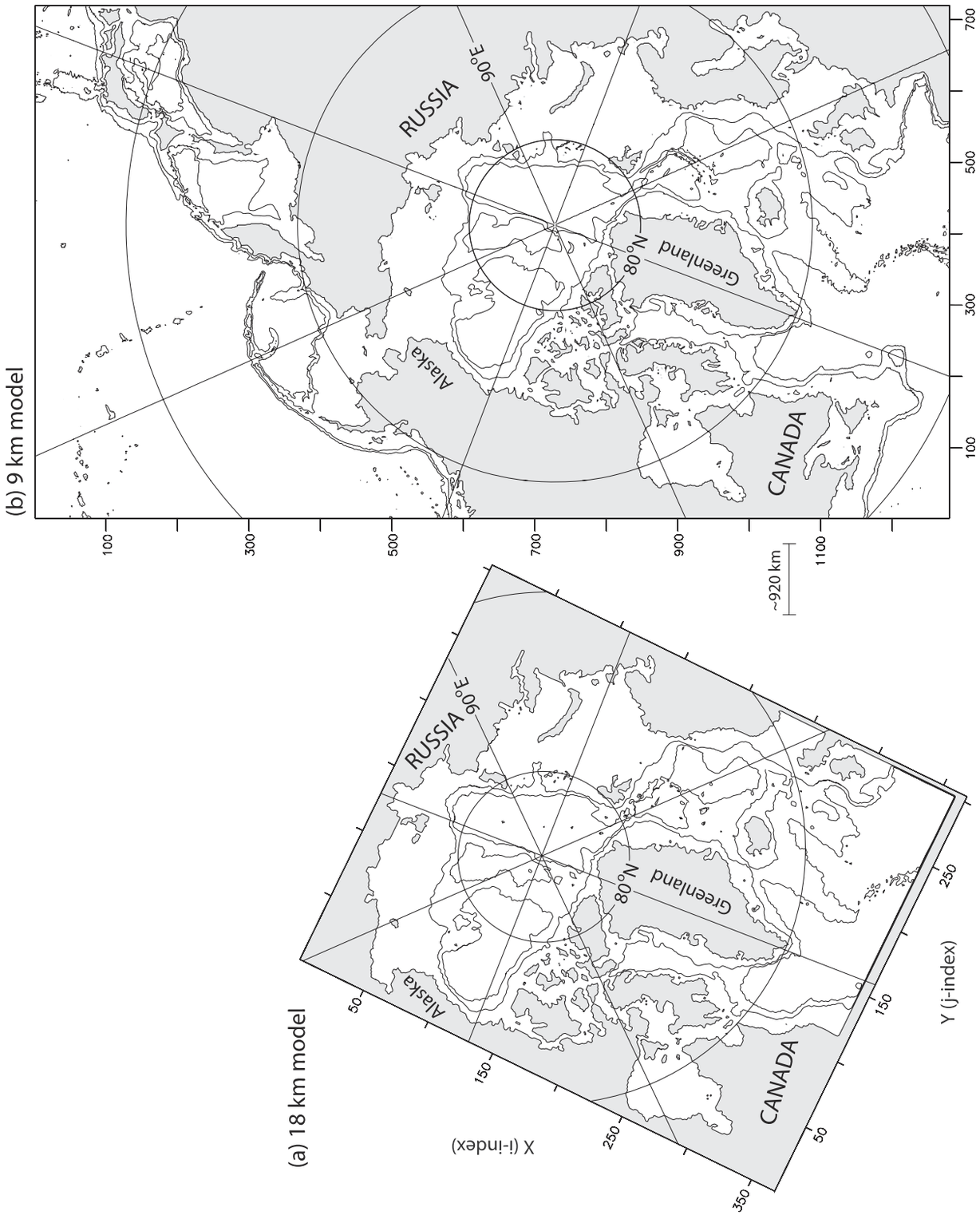
(b) 9 km model
RUSSIA
90°E
Greenland
80°N
Alaska
CANADA
100
300
500
700
900
1100
~920 km
(a) 18 km model
RUSSIA
90°E
Greenland
80°N
Alaska
CANADA
50
150
250
350
X (i-index)
Y (j-index)

Table 1. The 18-km (PCAP) and 9-km (NAME) Model Configurations and Key Parameters. Bdry-boundary, rpt-repeat, Sal-Salinity, pe-processing elements, PHC-Polarscience Center Hydrographic Climatology, ASRC-Arctic Region Supercomputing Center, ETOPO5-5-minute Gridded Global Relief Data from the National Oceanic and Atmospheric Administration.

Parameter		18-km Model	9-km Model
ocean model		LANL POP, free surface	LANL POP, free surface
ice model		Hibler (1979)	Hibler (1979)
horizontal grid		368×304	1280×720
vertical levels		30	45
bathymetry		IBCAO + ETOPO5	modified ETOPO5/IBCAO
initialization fields		PHC 2.0	PHC 1.0
atmospheric forcing		ECMWF	ECMWF
restoring fields	surface Lat. Bdry	PHC 2.0 monthly mean PHC 2.0 annual mean	PHC 2.0 monthly mean PHC 1.0 annual mean
restoring timescale	surface Lat. Bdry	Temp (365 d), Sal (120 d) (0–20m) 30 d	Temp/Sal (30 d) (0–5m) 10 d
timestep	ocean ice	20 min 120 min	8 min 48 min
horizontal diffusion coefficients	tracer	-4.00×10^{18}	-5.00×10^{17}
	momentum	-1.00×10^{19}	-1.25×10^{18}
vertical diffusion coefficients	background diffusion	0.1	0.05
	background viscosity	1	0.2
spinup integration completed		10-yr rpt 1979–1993 mean, 3 × 1979–1981 cycle (9 yr)	27-yr rpt 1979–1993 mn, 6 yr rpt 1979, 3 × 1979–1981 cycle (9 yr)
diagnostic integration completed		1979–1998	1979–2004
approximate integration time		~28 h/yr on 64 pe, ARSC T3E-900	~168 h/yr on 128 pe, ARSC T3E-900

The initial question: "Is the 9-km model better at simulating ocean and sea-ice dynamics and distribution of properties than the 18-km model?" can be answered with a qualified yes. Yes, in that better representation of the bathymetry has an immediate positive impact on the modeled circulation in several regions of the Arctic Ocean and its adjacent seas, where bathymetry is the controlling factor, such as the Barents Sea, the Chukchi Sea, and the Canadian Arctic Archipelago (CAA). Another yes, in that several narrow boundary currents that were absent or poorly represented in the 18-km model appear or become stronger and better defined in the 9-km model. An example of this will be shown in the Labrador Sea. Another yes, in that volume transports through Bering Strait, Fram Strait, and the Barents Sea are approaching observed values [*Clement et al*., 2005; *Maslowski et al.*, 2004], with the acknowledgment that even at ~9-km resolution, transport through the CAA is still possibly underrepresented. Finally, the ability of the 9-km model to reasonably represent eddy kinetic energy in the southern Labrador Sea and the Gulf of Alaska and to decrease the gap between modeled and observed values in the northern Labrador Sea from a factor of 10 to a factor of 1.22 indicates greater skill at simulating ocean energy levels, which in many regions determine observed conditions.

The representation of certain aspects of Arctic Ocean and sea ice characteristics are significantly improved in the 9-km model [NPS Arctic Modeling Effort or (NAME)] when compared with output from a previous 18-km model [Parallel Coupled Arctic Program or (PCAP)]. However, there are unknowns and shortcomings in the simulation of certain features that the 9-km model shares with the 18-km version, such as the representation of bottom boundary layer or tidally induced regional mixing and currents, verification of which is made difficult by a lack of observational data. The focus in this chapter will be to illustrate how representation

Figure 1. The 18-km PCAP model domain (a) and 9-km NAME model domain (b). The 18-km model image has been rotated 26°. Approximate distance scale is equivalent to one hundred 9-km model grid points and fifty 18-km model grid points. The 500- and 2500-m contours are shown in black.

of EKE in the pan-Arctic region has been improved because of the resolution increase.

The most significant finding is that inadequately resolving the basic large scale circulation can adversely impact a model's ability to properly represent water mass formation, distribution, and interactions due to advection, which will then impact heat, salt, and possibly mass balances. Underrepresentation of eddies and eddy kinetic energy will also impact the transport and mixing of water mass properties. In essence, improvements gained through perfecting subgrid-scale parameterizations will not help coarser models because improper representation of the circulation will inhibit or prevent water mass interactions. As shown by *Siegel et al*. [2001], eddy kinetic energy and the generation of eddies increase with increases in resolution, and at higher resolutions the rate of increase slows somewhat. Their highest resolution experiment, a 1.56-km resolution wind-driven, closed-basin, quasi-geostrophic ocean model, is approximately six times the resolution of the 9-km model discussed in this report. This indicates further increases in resolution should continue to result in improvements in the representation of mesoscale and smaller scale processes in the Arctic Ocean.

The 18-km model used here is similar to that used by *Maslowski et al*. [2000, 2001] except for the bathymetry dataset, which was derived from the International Bathymetric Chart of the Arctic Ocean (IBCAO) [*Jakobsson et al*., 2000] and interpolated onto the model grid [*Marble*, 2001].

The remainder of this chapter will first briefly discuss improvements gained through the increase in resolution in the following order: (1) representation of the bathymetry and circulation in regions where bathymetry is the major controlling factor; (2) the representation of shelf break and coastal boundary currents; and (3) the increase in eddies and eddy kinetic energy noted in the 9-km model. Analyses of modeled eddies and EKE are organized in three separate regions: subpolar North Atlantic, subpolar North Pacific, and the Arctic Ocean. The choice of model output used was made based on its availability at the time of particular regional analyses. Every effort has been made to compare equivalent depths and regions. The NAME model domain is shifted ~26° to the west when compared to that of PCAP. Therefore, 18-km model images, when placed next to 9-km model images, have been rotated 26°.

2. SUBPOLAR NORTH ATLANTIC

2.1. Labrador, Nordic, and Barents Seas

2.1.1. Bathymetry Impacts. It is obvious that increased resolution will result in improved representation of the geography and bathymetry within a model domain. Higher sampling along a coastline or a vertical section will capture higher frequency variations in that profile. Some smoothing will occur and many small features will still be missed, but as resolution increases, features attain a more realistic shape. What is less clear is what resolution will ensure enough of the horizontal and vertical variations have been captured to accurately simulate the circulation and mass balances.

As discussed by *Maslowski et al*. [2004], the 9-km model exhibits considerable skill in representing the mean circulation in the Barents Sea, a region where bathymetry is a major controlling factor in the circulation [e.g., *Pfirman et al*., 1994]. Circulation in the PCAP Barents Sea (Plate 1a) exhibits many similar features to the 9-km model. Yet due to poorer vertical resolution and the resultant representation of the bathymetry in the Barents Sea, specifically Great Bank and Central Bank, PCAP displays pathways that are not in agreement with the observed circulation in the Barents Sea [*Ozhigin et al*., 2000] nor with the modeled circulation from the NAME model (Plate 1b). There appear to be two paths the warm Atlantic Water follows through the Barents Sea, with larger velocities and more concentrated currents along the northern path (Plate 1a). This dynamical difference has significant physical implications on volume and property fluxes and on the nature of the water mass transformation that takes place in the Barents Sea. The placement of the primary pathway of warm Atlantic Water through the Barents Sea farther to the north also impacts the oceanic frontal structure as well as the ice edge, which in turn force the region's ecosystem.

2.1.2. Boundary Current. Boundary currents are crucial in the transport of volume, heat, salt, and freshwater throughout the Arctic Ocean and the subpolar seas [*Rudels*, 1987; *Aagaard*, 1989, *Rudels et al*., 1994]. The Labrador Sea plays a key role in the global thermohaline circulation as one of the few deepwater formation regions in the world [*Broecker*, 1991; *Skyllingstad et al*., 1991]. Furthermore, variations in the transport of cold, fresh Arctic Ocean outflow, as well as sea-ice and icebergs, by boundary currents such as the East and West Greenland Currents, the Baffin Current, and the Labrador Current precondition the Greenland Sea and the Labrador Sea for deep convection and deep water formation. Large freshwater outflows can alter deep convection in either area [*Dickson et al*., 1988, 1996; *Visbeck et al.*, 1995]; therefore, proper representation of these currents is crucial.

Labrador Sea boundary currents are narrower and stronger in the 9-km model as represented by the mean velocity in the top 180 m when compared to the 18-km model (Plate 2). Improved representation of northward flow through Davis Strait is apparent as well as bathymetric effects on the

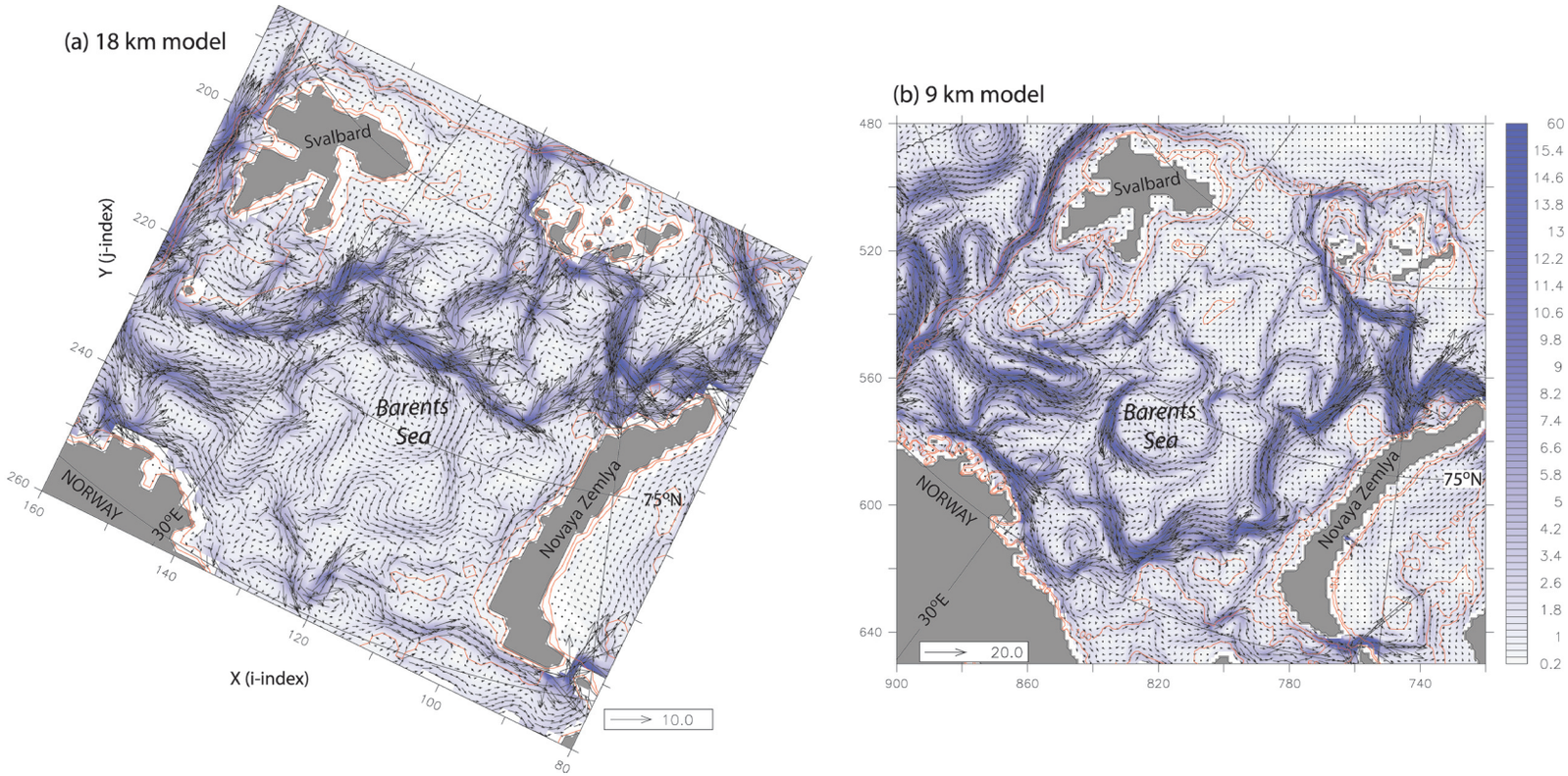

Plate 1. Distribution of 1980 annual mean velocity (cm/s) in the Barents Sea. (a) PCAP, 0–225 m (model levels 1–7), every vector is plotted; (b) NAME, 0–223 m (model levels 1–15), every other vector is plotted. Background shading is current speed (cm/s) and is the same for both model images. Note the differing vector scales.

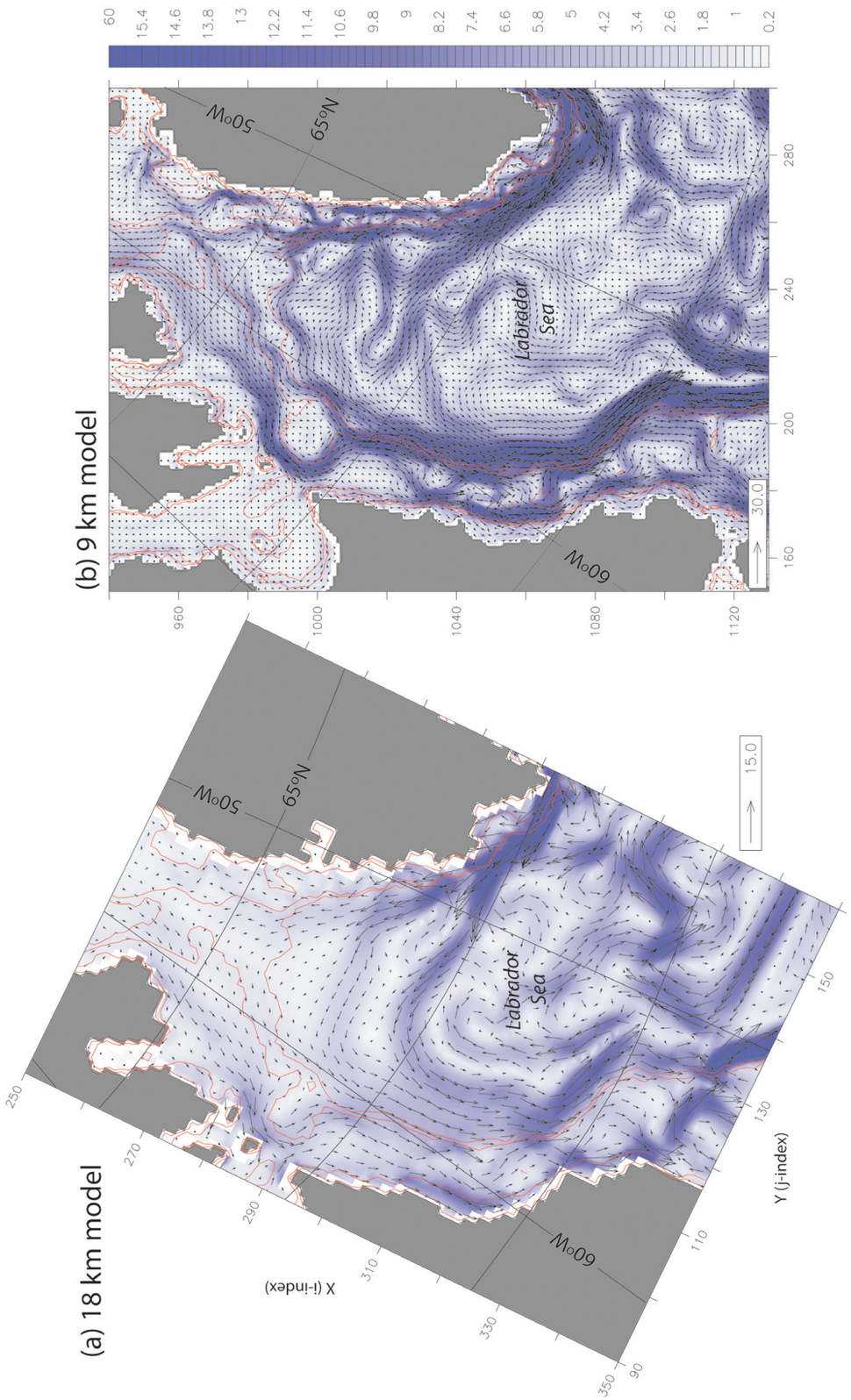

Plate 2. Distribution of 1980 annual mean velocity (cm/s) in the Labrador Sea. (a) PCAP, 0–180 m (model levels 1–6); (b) NAME, 0–183 m (model levels 1–14). Every other vector is plotted. Background shading as in Plate 1. Note the differing vector scales.

southerly flowing Baffin Land/Labrador Current. The width of the western branch of the Baffin Land/Labrador Current traveling around the 500-m contour at the mouth of Hudson Strait is ~50 km in the 9-km model versus ~100 km in the 18-km model. The separation of the West Greenland Current into several branches of westward flow across the Labrador Sea [*Cuny et al.*, 2002] is more distinct, as are the interactions between the current along the Labrador coast and the shelf break current. The proximity of the 18-km model boundary and modifications made to the coastline must be taken into account in the behavior of the coastal current south of 55°N and representation of the northward intrusion of North Atlantic Current meanders into the Labrador Sea (Plate 2a).

2.1.3. Eddies and Eddy Kinetic Energy. Eddies play a significant role in oceanic circulation in that they can result in the propagation of significantly different water masses outside of their place of origination [*Gent et al.,* 1995] and their dissipation transfers momentum between length scales and transfers properties between water masses. Their size is governed by the scale of the Rossby deformation radius defined as:

$$R = (g'D)^{1/2}/f \tag{1}$$

where $g' = g\Delta\rho/\rho$ is the reduced gravitational acceleration, g is the acceleration due to gravity, $\Delta\rho/\rho$ is a characteristic density difference ratio for the fluid over the vertical scale of motion D, and f is the Coriolis acceleration [*Pedlosky*, 1987]. In the Arctic Ocean, due to high latitude (i.e., large f) and relatively weak vertical stratification, this scale, hence the size of eddies, is on the order of 0 (10 km) or less [*Manley and Hunkins*, 1985; *D'Asaro*, 1988; *Plueddemann et al*.,1998; *Pickart et al*., 2005]. In the sub-Arctic regions, the eddy radius increases to 20 km or more in the Labrador Sea [e.g., *Pickart et al*., 1996] and 25–100 km in the Bering Sea/Gulf of Alaska [*Okkonen*, 1993; *Schumacher and Stabeno*, 1994; *Stabeno and Reid*, 1994; *Crawford et al*., 2000; *Ladd et al*., 2007].

Proper eddy parameterization in coarser resolution models is found to be important insofar as eddy-topography interactions contribute to propelling and sustaining narrow boundary currents [*Nazarenko et al*., 1997, 1998]. *Semtner and Chervin* [1992] presented results from the first eddy-resolving global ocean circulation model and since then, further improvements in the efficiency of model codes and supercomputer capabilities have allowed continued resolution increases in many applications, which have broadened our view of the intensity and distribution of eddies in the oceans. These resolution increases do come at considerable computational cost (cf. Table 1 for this limited regional example). There is a vigorous and continuing discussion about finding the proper balance between resolution increases and parameterizations that will allow long integrations to accurately simulate circulation at multiple length scales and maintain mass and property balances.

Because the high spatial resolution of the 9-km model allows analysis of eddies theoretically down to a scale of ~30 km, we investigate the distribution of eddy kinetic energy (defined as EKE = $(u'^2 + v'^2)/2$, following *Stevens and Kilworth* [1992]). These calculations are done for monthly and daily fluctuations, referred to the annual mean. The monthly average data sets used in EKE calculations represent the average of all timesteps in that month (roughly 5400 timesteps), whereas a daily snapshot represents the last timestep out of the approximately 180 timesteps during one day. In addition, due to storage and integration time considerations, the daily snapshots contain only surface velocity components among other limited variables.

The annual mean velocity components, $\overline{u}$ and $\overline{v}$, were subtracted from the daily velocity values or monthly average velocity values to obtain u' and v'. EKE was calculated for the region including the northern Norwegian, Greenland, and Barents Seas. The annual mean surface EKE for the 9-km model, calculated from monthly average output, was found to represent approximately 15% of the annual mean surface EKE calculated from daily snapshots (8.40 cm^2/s^2 versus 54.53 cm^2/s^2; with standard deviations about the means of 12.6 cm^2/s^2 versus 70.2 cm^2/s^2, respectively).

A comparison of the EKE calculated in a similar region using output from the 18-km resolution model [*Maslowski et al.,* 2000] shows area-averaged monthly mean EKE in the 9-km model exceeds EKE in the 18-km model by a factor of 5.

A comparison of model 1993–1997 mean surface EKE with similar multiyear mean EKE values deduced from observed surface drifter data [*Cuny et al.,* 2002] indicates that the 9-km model is able to reproduce the geographic distribution of EKE maxima similar to that observed (Plate 3). Model EKE values match those observed in a northern extension of the North Atlantic Current, the lower right corner of Plates 3a and 3b. Farther north, however, the model EKE values are roughly 20–30% lower than the observed values. The maximum daily surface EKE in the region in Plate 3a is ~1542 cm^2/s^2, the annual mean ~113 cm^2/s^2 with a standard deviation about the mean of 168 cm^2/s^2.

The difference in EKE in the northern Labrador Sea may be due to differences in the atmospheric forcing between daily-averaged, relatively low-resolution, and spatially smoothed European Center for Medium-Range Weather Forecasting (ECMWF) data prescribed in the model and the real conditions experienced by surface drifters. Another potential cause of the difference may be due to model resolution. As latitude increases and vertical density stratification decreases, the

internal Rossby radius decreases. The North Atlantic Current is well stratified in comparison to the nearly vertically homogeneous waters of the northern Labrador Sea, thus the Rossby radius within the North Atlantic Current is larger and the model is able to reproduce the observed eddy kinetic energy. That the 9-km model is able to reproduce the observed spatial distribution and magnitudes of EKE is quite significant, especially when compared to EKE values calculated in a similar region using output from a coarser resolution ~18-km model. The 9-km model values are 10 times larger than the 18-km model values.

Results presented above indicate that the 9-km model was able to accurately represent the mean levels of EKE observed in the southern Labrador Sea. Whether the difference between modeled and observed EKE in the northern Labrador Sea is a function of latitude and vertical stratification or the significant differences between the model and actual atmospheric forcing adds uncertainty to any conclusions drawn about 9-km model performance in this region. However, comparison of snapshots of EKE in the top ~45 m of the Labrador Sea clearly indicates that EKE is significantly underrepresented in the 18-km model (Plate 4). The southern maximum in EKE in the 18-km model (Plate 4a) corresponds to energy within a branch of the North Atlantic Current that extends to the north, then east. Geographic distribution of EKE maxima in the 9-km model are in reasonable agreement with the observed means (Plate 4b). The underrepresentation of EKE in the 18-km model may cause insufficient mixing of water from the West Greenland Current with surface water in the central Labrador Sea. This would in turn impact the degree of stratification, which would affect overturning and deepwater formation.

Dramatic differences exist in the distribution of 0- to 45-m eddy kinetic energy in the Nordic Seas between the two models (Plate 5). When viewed as an aggregate, the concentration of increased EKE in the 9-km model appears to define the path of the North Atlantic Current passing south of Iceland, and the Norwegian Atlantic Current as it travels north, along the west coast of Norway (Plate 5b). Indication of such a pathway is absent in the distribution of 18-km model EKE (Plate 5a). There is an order-of-magnitude difference in EKE statistics computed for the regional snapshots discussed previously (Table 2) as well as in the statistics computed for similar regional annual mean surface (0–20 m, PCAP level 1; 0–5 m, NAME level 1) EKE values (not shown).

The 9-km EKE in the model is still underrepresented due to inadequate resolution, the use of mean atmospheric forcing to drive the model during spinup, and the monthly mean output used in many of these calculations. The internal Rossby radius of deformation is about 6 km in the St. Anna Trough (U. Schauer, personal communication) and a model would require a grid cell spacing on the order of 1–2 km to be able to reasonably resolve features of that scale.

Considerable seasonal variability is noted in the 9-km model EKE distribution in the Labrador Sea (Plate 6) in qualitative agreement with limited observational estimates [*White and Heywood,* 1995]. The winter EKE maximum in the Labrador Sea, the majority of which remains ice-free year round, is due to an increase in storm activity during the winter months. The daily EKE maximum in the Labrador Sea in wintertime is roughly 25% larger than the summer maximum, 2400.1 versus 1919.8 cm^2/s^2, respectively. The Labrador Sea winter mean EKE, 135.6 cm^2/s^2, is ~1.7 times the summer mean of 80.2 cm^2/s^{-2} and there is more variability in the values in the wintertime, with winter standard deviation about the mean ~205 cm^2/s^2 and summer standard deviation about the mean ~150 cm^2/s^2.

3. SUBPOLAR NORTH PACIFIC

3.1. Gulf of Alaska

The 18-km (PCAP) model domain did not include the subpolar North Pacific (Figure 1), therefore we analyze and present results from the 9-km (NAME) model in this section on the Gulf of Alaska, and the following section will focus on the Bering Sea. We examine individual eddies and their frequency, along with associated impacts on the surrounding water masses.

Observations and models have identified the region south of the Aleutian Island Arc, in the vicinity of the Alaskan Stream, as an area of high eddy activity [*Maslowski et al*., 2008; *Crawford et al*., 2000; *Reed and Stabeno*, 1999; *Okkonen*, 1992]. Large (mean diameter of 160 km) and long-lived (1–3 years) anticyclonic eddies have been observed propagating along the Alaskan Stream at an average speed of 2.5 km d^{-1} [*Crawford et al*., 2000]. Sea surface height anomalies (SSHA) approached 72 cm. Similarly, model results show anticyclonic eddies with a mean diameter of 168 km and SSHA of 62 cm [*Maslowski et al*., 2008]. Using satellite altimetry, *Crawford et al*. [2000] recorded the presence of six anticyclonic eddies during a 6-year period (September 1992–September 1998). Over this same time frame, modeled SSHA also show six eddies propagating westward south of the Aleutian Island Arc (Figure 2).

Model simulations over a 25-year period (1979–2003) showed a total of 20 anticyclonic eddies crossed a north-south line (~173.5°W) in the Alaskan Stream just east and south of Amukta Pass [*Maslowski et al*., 2008]. These eddies, with SSHA greater than 30 cm, make for an average of 0.8 per year. Twelve of the 20 eddies had SSHA greater than 50 cm for an average of 0.5 per year.

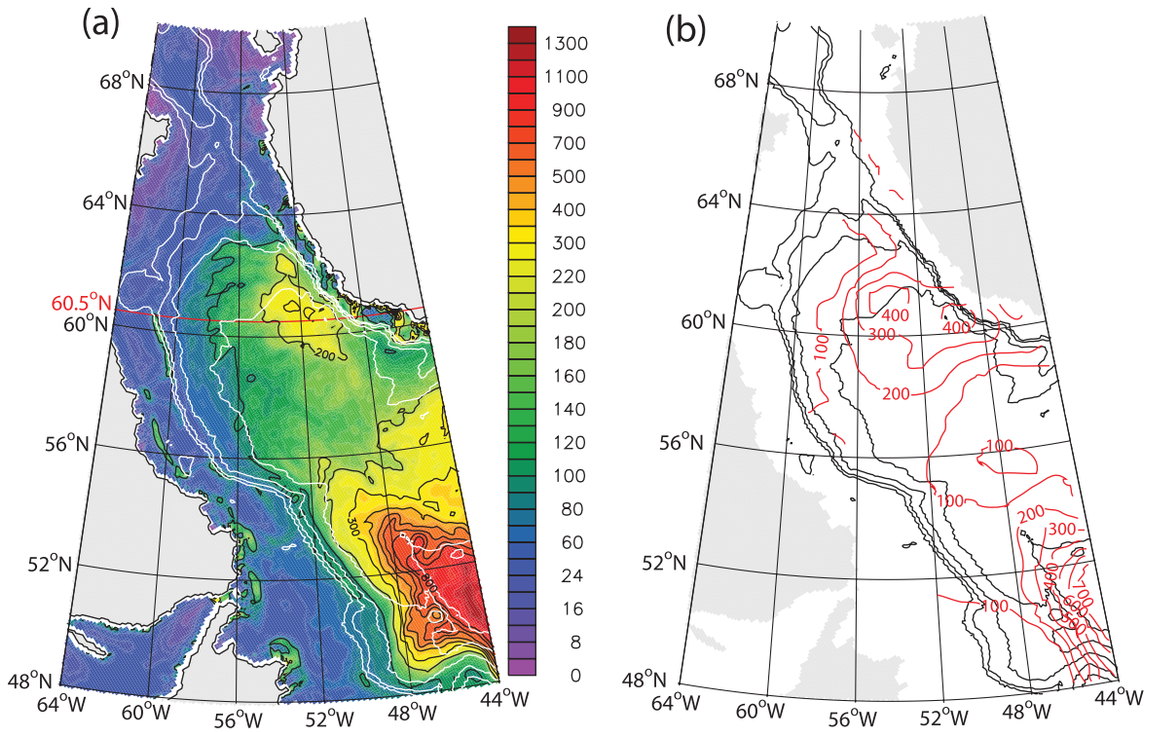

Plate 3. Horizontal distribution of eddy kinetic energy (cm^2/s^2) in the Labrador Sea. (a) 1993–1997 annual mean, 0–5 m (model level 1) calculated from daily model output. EKE contours 100, 200, 300, 400, 500, 600, 700, and 800 cm^2/s^2 in black. (b) Eddy kinetic energy deduced from surface drifter data released in North Atlantic Ocean and Labrador Sea in during 1993–1997. (After Figure 7 from *Cuny et al*. [2002].)

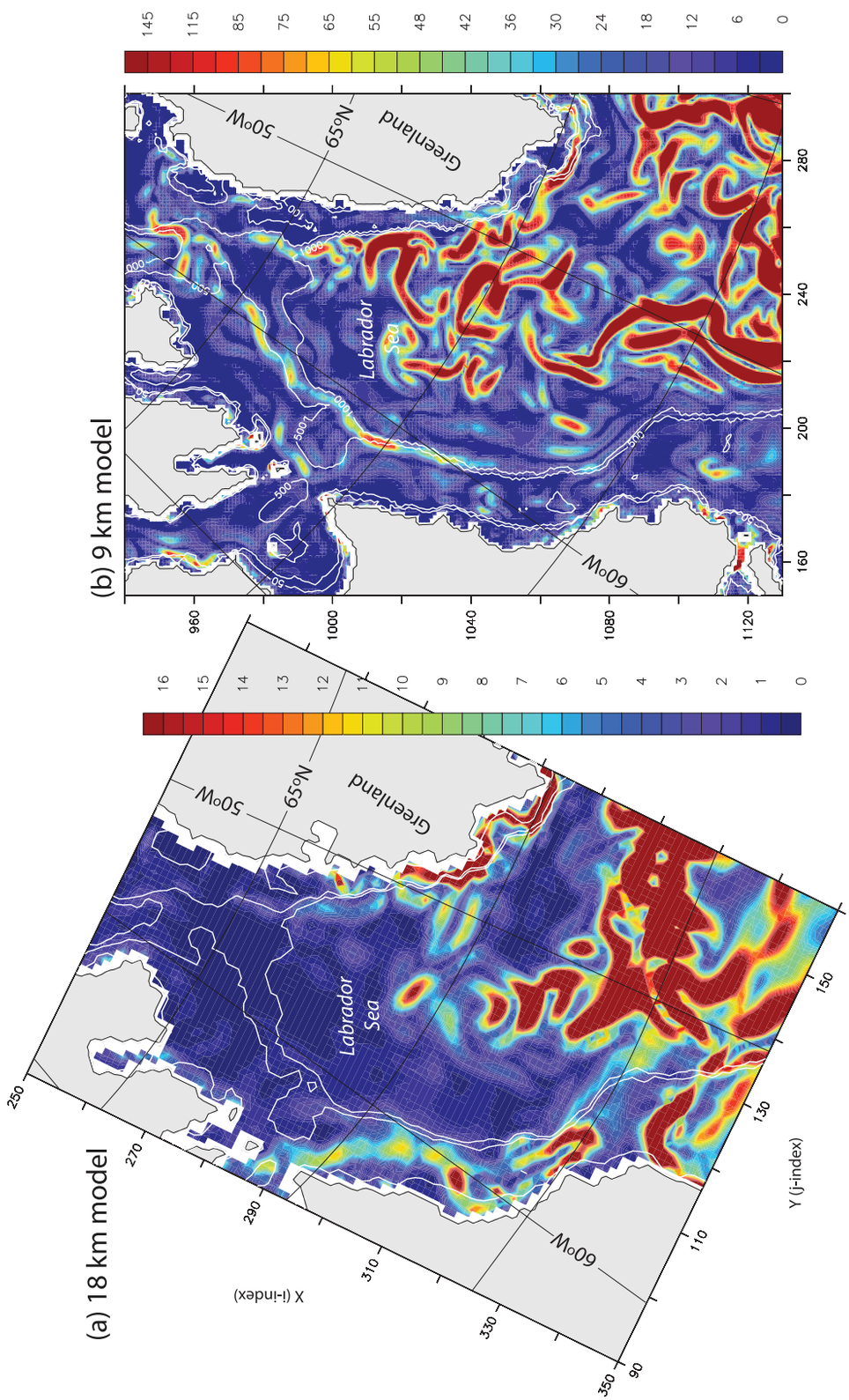

Plate 4. August 1980 snapshot of surface layer eddy kinetic energy (cm^2/s^2) in the Labrador Sea: (a) PCAP, 0–45 m (model levels 1–2); (b) NAME, 0–43 m (model levels 1–7). Note the different shading scales.

The propagation of one of these large eddies affects the flow of the Alaskan Stream by shifting the westward velocity core offshore by 70–155 km, depending on the size (or diameter) of the eddy and the particular location along the Aleutian Island Arc. As an example, Figure 3 shows the offshore displacement of the Alaskan Stream just east and south of Amukta Pass (~173.5°W) in December 1993 due to an eddy. (This eddy is shown when it was further upstream in April 1993 in Figure 2 as eddy 2.) The 25-year mean velocity structure shows speeds up to 70 cm/s at the surface, with speeds exceeding 5 cm/s as deep as 2000 m. The velocity core is typically located near the slope; however, as Figure 3 shows, an eddy can cause a large horizontal displacement, in this case ~155 km offshore. During the eddy passage, the maximum surface speed slows to 55 cm/s. However, the total westward volume transport through this cross section is actually higher during eddy passage (60 Sv) compared to the long-term mean (53 Sv), due to the widening and deepening of the velocity core. In fact, speeds of more than 5 cm/s reach the bottom at a depth of 5000 m during eddy passage.

This eddy, which we use as an example, was in the vicinity of Amukta Pass from October 1993 to February 1994 and caused significant changes in the salinity structure of the region over this period. During the eddy's approach, low salinity waters that typically lie over the shelf are drawn offshore to the south by more than 200 km. In addition, the eddy is responsible for bringing relatively salty water up the slope and into Amukta Pass. During the passage of the eddy, monthly mean volume transport and salt flux anomalies through Amukta Pass reached 1.25 Sv and 40 million kg/s, respectively. Below the euphotic zone, salinity is positively correlated with nutrient concentrations (P. Stabeno, personal communication). This means that eddy-induced upwelling along the slope has the potential to supply the Aleutian shelves with nutrient-rich water.

3.2. Bering Sea

Eddies in the Bering Sea are primarily found in the basin and along the slope in the Bering Slope Current (BSC) region. Our model results and observational data [*Okkonen*, 1993] indicate that the lifetimes of eddies in the Bering Sea are typically a few months to a year and tend to be shorter than those in the Gulf of Alaska, which range from 1 to 3 years. Another difference between these two regions, based on model results, is the presence of both cyclonic and anticyclonic eddies in the Bering Sea basin, whereas the Alaskan Stream is more prone to large anticyclonic features.

To better understand the ability of the model to represent realistic energies, we compare TOPEX altimeter observations along orbital ground track D79 (located along the shelf break region of the central Bering Sea) with model results for 1994–2001. Figure 4 shows power spectra of observed SSHA along this TOPEX ground track and modeled SSHA interpolated at points corresponding to the TOPEX ground track locations. At longer wavelengths (greater than ~200 km), the observed and modeled spectra exhibit similar energies. However, the modeled energy drops off more rapidly than the observations at shorter wavelengths, causing the spectra to diverge. Peaks at ~40 and ~20 km can be seen in the model spectrum and an increasing amount of noise shows up at shorter wavelengths in the altimeter spectrum. Interpolating 9-km gridded model output to the 6.2-km TOPEX sample spacing likely caused spatial aliasing, which shows up as peaks at the shortest wavelengths in the model spectrum.

The BSC is a predominant feature of the Bering Sea; however, this current has been described as more of a system of eddies rather than a continuous current [*Okkonen,* 1993]. Model results show eddies with diameters ranging from 90 to 325 km are frequently found in the Bering Sea basin, with a high concentration along the downstream portion of the Bering Slope Current region to the northwest [*Clement Kinney et al*., 2008]. For example, in November 1993, a cyclonic eddy with a diameter of 145 km is located just south of Zhemchug Canyon (ZC) (Figure 5). We can also see an anticyclonic feature adjacent to the cyclonic eddy, suggesting dipole formation due to the presence of the canyon.

The eddy's presence in the canyon strongly affects the local distribution of salinity. Vertical sections of salinity anomalies at BSC (not shown) and ZC (Plate 7) show high salinity water being upwelled and pushed onto the shelf when the eddy is present, during November 1993. Monthly mean salinity anomalies approach 0.12 in the surface water and are even higher near bottom (up to 0.18). Velocities are relatively strong (monthly mean up to 12 cm/s) and directed on-shelf.

It has been suggested [*Paluszkiewicz and Niebauer*, 1984; *Okkonen*, 1993; *Mizobata et al*., 2006] that topographic planetary waves generated by baroclinic instabilities are responsible for eddy generation along the Bering slope. The modeled eddy described above had a diameter of 145 km and period of ~90 days, which is similar to observations made by *Paluszkiewicz and Niebauer* [1984; 140 km/84 days] and *Okkonen* [1993; 184 km/72 days]. Based on these results and the assumption that deep Bering Sea water is high in nutrient concentrations [*Clement et al*., 2005], it can be inferred that mesoscale eddies are responsible for providing the Bering Sea shelf with nutrient-rich water from the basin. The location, duration, and frequency of eddy activity would then be highly important to ecosystems on the shelf. As seen in the model results, the Zhemchug Canyon region appears to be a prime location for eddy activity and subsequent upwelling of salty, nutrient-rich water.

4. ARCTIC

4.1. Chukchi Sea, Beaufort Sea, and Canada Basin

The Arctic Ice Dynamics Joint Experiment (AIOJEX) of 1972 was the first study to identify subsurface mesoscale eddies in the Arctic Ocean [*Manley and Hunkins*, 1985]. Over the 14-month time frame, a total of 127 eddies were identified between 50 and 300 m depth. They ranged in diameter from 10 to 20 km and were predominantly anticyclonic with an anticyclonic/cyclonic eddies ratio of 5:2. Later work by *D'Asaro* [1988] revealed the presence of vertical pairs of counterrotating eddies in the Beaufort Sea. Although poorly sampled, it was observed twice that anticyclonic eddies in the upper water column (but below 50 m) were associated with deep cyclonic features. *Plueddemann et al*. [1998] were able to clearly observe 10 eddies in 23 months of data collected by a drifting buoy equipped with an ADCP in the Beaufort Gyre. Again, a predominance of anticyclonic eddies was noted (9 of 10); however, no observations of a deep counterrotating eddy were made, possibly due to a lack of samples in deep enough water. Modeling work by *Chao and Shaw* [1996] showed how a pair of counterrotating eddies might occur in the Beaufort Sea. A pulse of either lower or higher density water could create a shallow eddy with a deep counterrotating eddy; however, the shallow one is more quickly dissipated due to surface friction exerted by sea ice. *Pickart et al*. [2005] suggest two general mechanisms for formation of eddies found in the Canada Basin: current-topographic interactions (primarily in Barrow Canyon) and hydrodynamic instability. In this section, we will first examine the energetics of the Chukchi and Beaufort shelves and then later describe eddies found in deeper waters of the slope and basin. We use results from the 9-km model instead of the 18-km model, due to its ability to better represent smaller features and the small Rossby radius of deformation found in the Arctic Ocean, as noted earlier.

Modeled eddy kinetic energy at 20- to 26-m depth on the Chukchi and Beaufort shelves from the 9-km model is highest during the summer and autumn (Plate 8). Values of more than 500 cm^2/s^2 are found in shallow water (<50 m deep) in Bering Strait and near Point Barrow. However, these high values of EKE are likely due in large part to fluctuations in current speed and also current reversals, rather than actual mesoscale eddies.

More interestingly, EKE values up to 10 cm^2/s^2 are found along the Beaufort shelf break and in the Canada Basin throughout the year. In an attempt to more closely examine these features, we created animations of monthly "snaphots" of EKE for 5 years (1985–1989). "Snapshots" represent the last timestep of each month. Five-year mean (1985–1989) values of the horizontal components of velocity were used as the "long-term" mean in calculating the EKE. We completed the same exercise for several depth levels from 20–26 to 395–478 m. A typical EKE distribution is shown in Plate 9 for July 31, 1986, at 268–326 m. At least five anticyclonic and three cyclonic eddies are visible, with most present in the Western Beaufort Sea, especially near the Barrow Canyon outflow. Eddies that are located along the Beaufort slope appear to be associated with the Barrow Canyon, and are an important means of communication between the shelf and basin [*Pickart et al*., 2005]. In addition, there is a large anticyclone off the northeast corner of the Chukchi Cap. Eddies were commonly found inside the black box (Plate 9); therefore we examine the vertical structure of one of these eddies in the following paragraph.

After careful examination of the vertical structure of EKE over the 5-year period and over the entire water column, we found that it is sometimes possible to have a vertical pair of counterrotating eddies. Plate 10 shows EKE and velocity on November 30, 1985 (left), at three representative depth levels. The shallower, anticyclonic eddy is at ~15- to 100-m depth, with speeds up to 5 cm/s^{-1} and a diameter of ~75 km (Plate 10a). The lower, cyclonic eddy (Plate 10c) has a larger diameter (~110 km) and is found at depths from 150 to well below 400 m. Rotational speeds are slightly higher for the cyclonic eddy, reaching 5.5 cm/s^{-1}.Weak and unorganized flow exists at depths ranging from 100 to 150 m between the two eddies. Six months later (on May 31, 1986), the shallow, anticyclonic eddy has dissipated, but the deeper cyclone remains intact (Plate 10). In fact, this eddy has a lifetime of 18 months versus only 6 months for the upper one, likely due to surface wind forcing and friction from the overlying sea ice [*Chao and Shaw*, 1996].

A vertical cross section of salinity and density (σ_θ) through these counterrotating eddies (along the black line shown in Plate 10) is shown in Plate 11. On November 30, 1985, in the upper 50 m, the doming of the isopycnals (and isohalines, as

Table 2. Eddy Kinetic Energy (cm/s) Statistics for the 0- to 45-m Regional Snapshots Presented in Plates 4 and 5

Model	Labrador Sea EKE			Nordic Seas EKE		
	Maximum	Mean	Std Dev	Maximum	Mean	Std Dev
PCAP58	132.50	4.90	9.20	269.40	4.70	13.30
PIPS	3998.00	70.40	203.70	4959.00	43.50	142.70

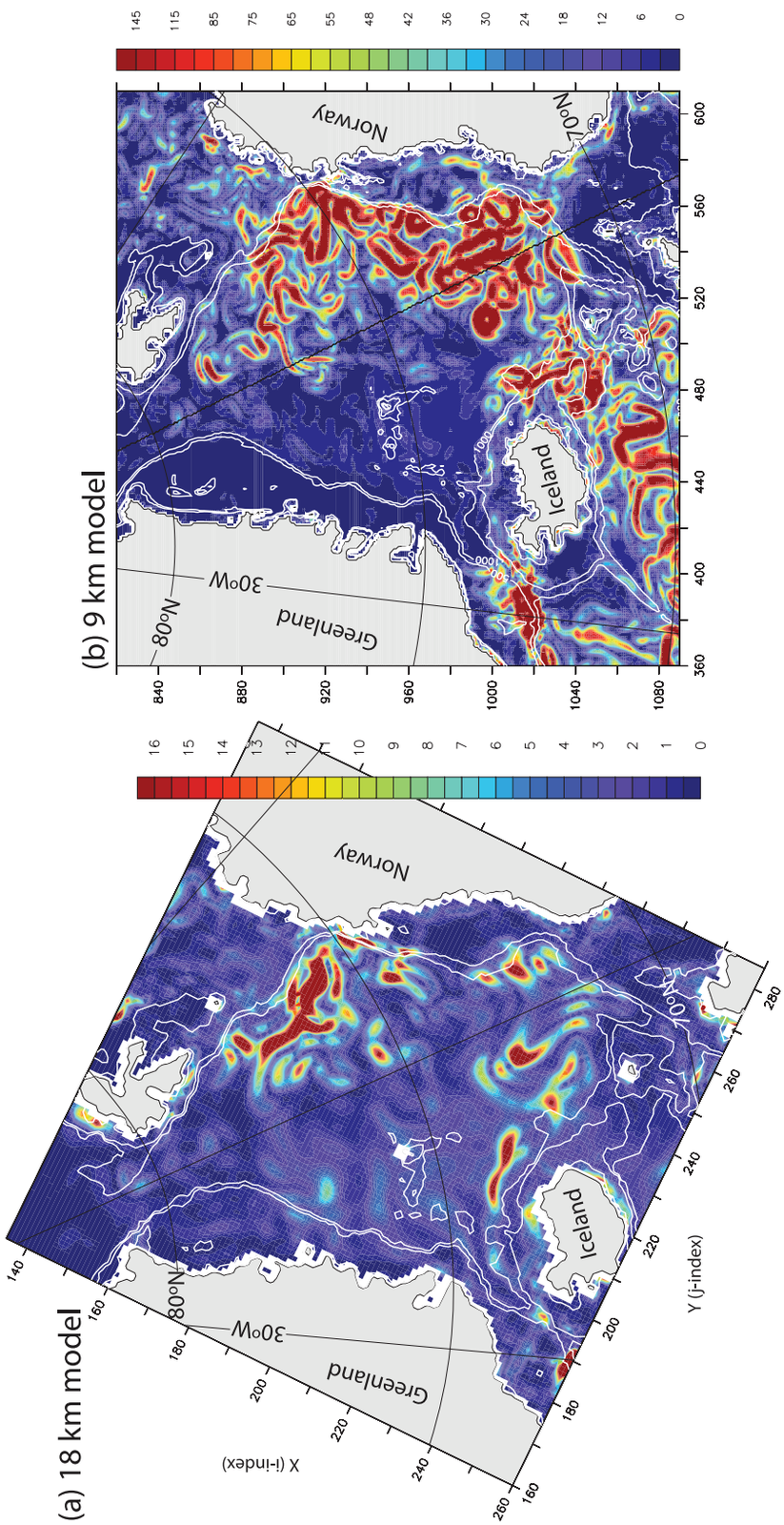

Plate 5. August 1980 snapshot of surface layer eddy kinetic energy (cm^2/s^2) in the Nordic (Greenland, Iceland, and Norwegian) Seas: (a) PCAP, 0–45 m (model levels 1–2); (b) NAME, 0–43 m (model levels 1–7). Note the different shading scales.

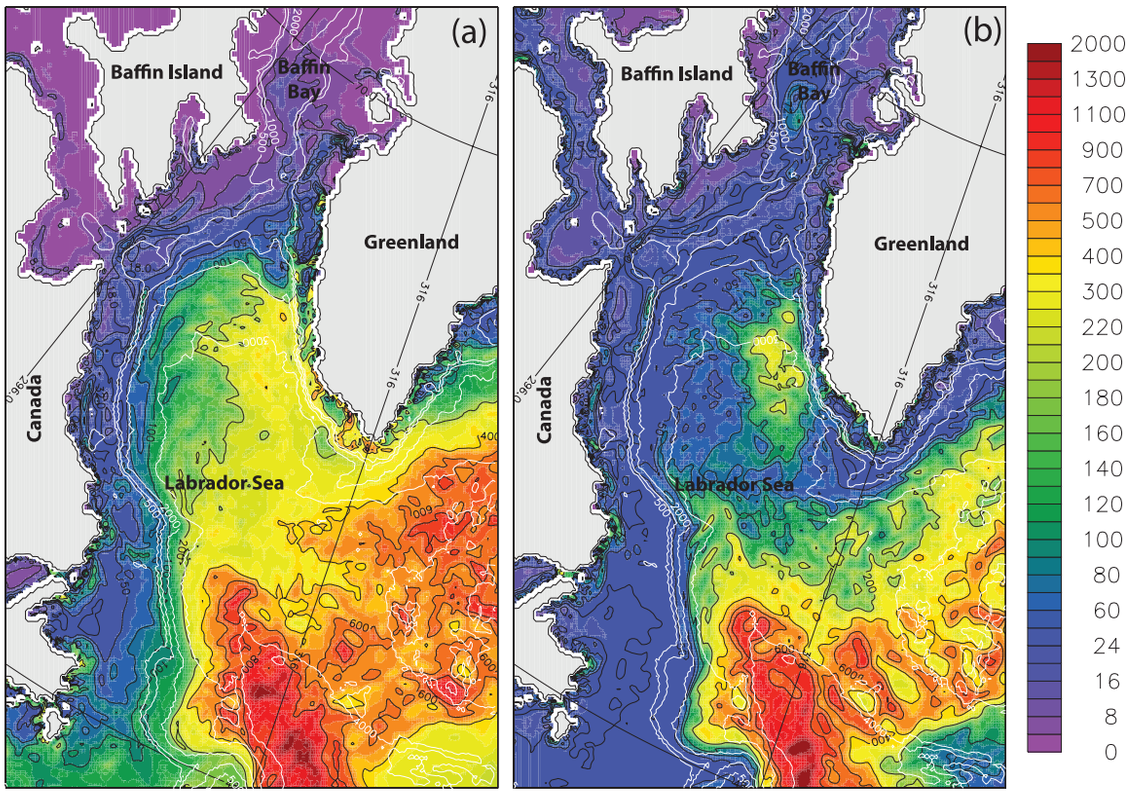

Plate 6. Horizontal distribution of surface (0–5 m, model level 1) 1993–1997 eddy kinetic energy (cm^2/s^2) in the Labrador Sea for different seasons: (a) winter (J-F-M) average; (b) summer (J-A-S) average. EKE contours: 8, 18, 32, 50, 72, 100, 200, 400, 600, and 800 cm^2/s^2.

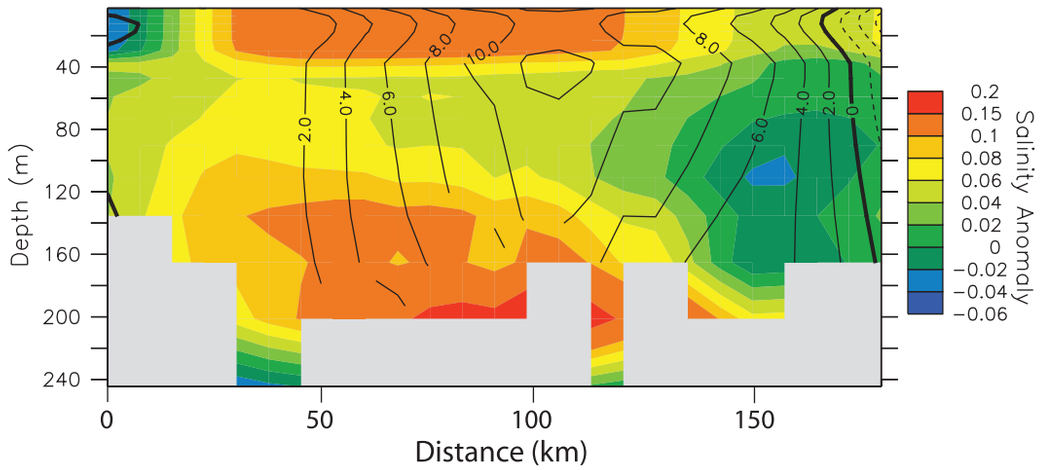

Plate 7. Vertical section of salinity anomaly across Zhemchug Canyon (section location shown in Figure 5) during November 1993. Contour lines indicate the across-slope velocity (positive onto the shelf; cm/s). Modified from *Clement Kinney et al*. [2008].

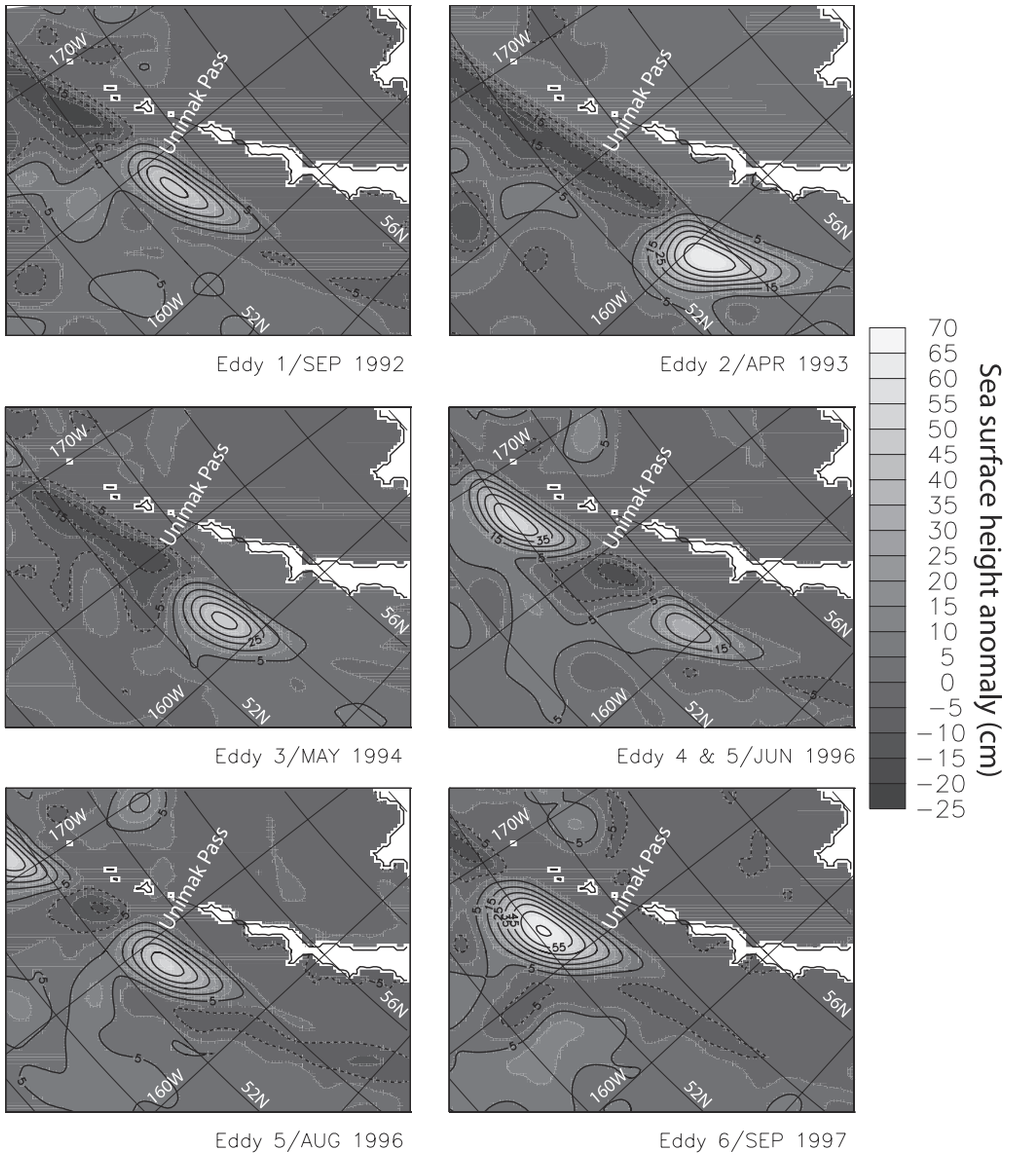

Figure 2. Modeled monthly mean sea surface height anomaly associated with six eddies propagating along the Alaskan Stream during the period September 1992 through September 1998. Shading represents the total SSHA (cm). Modified from *Maslowski, et al*. [2008].

well) is readily apparent, with vertical displacements up to ~20 m. In addition, sea surface height shows a local high centered over the eddy (not shown). A depression of the isopycnals and isohalines occurs below 50 m depth (likely due to the accumulation of water above) and shows even greater vertical displacements (up to 30 m). After the shallow eddy has dissipated on May 31, 1986, the upper water column is characterized by much flatter isopycnals and isohalines (Plate 11, right). However, below 150 m the depression of the isopycnals is still present, indicative of the cyclonic circulation that is seen in Plate 10f. The black dashed boxes in Plate 11 correspond to the three depth levels shown in Plate 10.

Modeled eddies occurred frequently throughout the 5-year period (1985–1989). However the diameters of these eddies were typically 80–150 km, which is significantly larger than observations (10–20 km) [*Manley and Hunkins*, 1985;

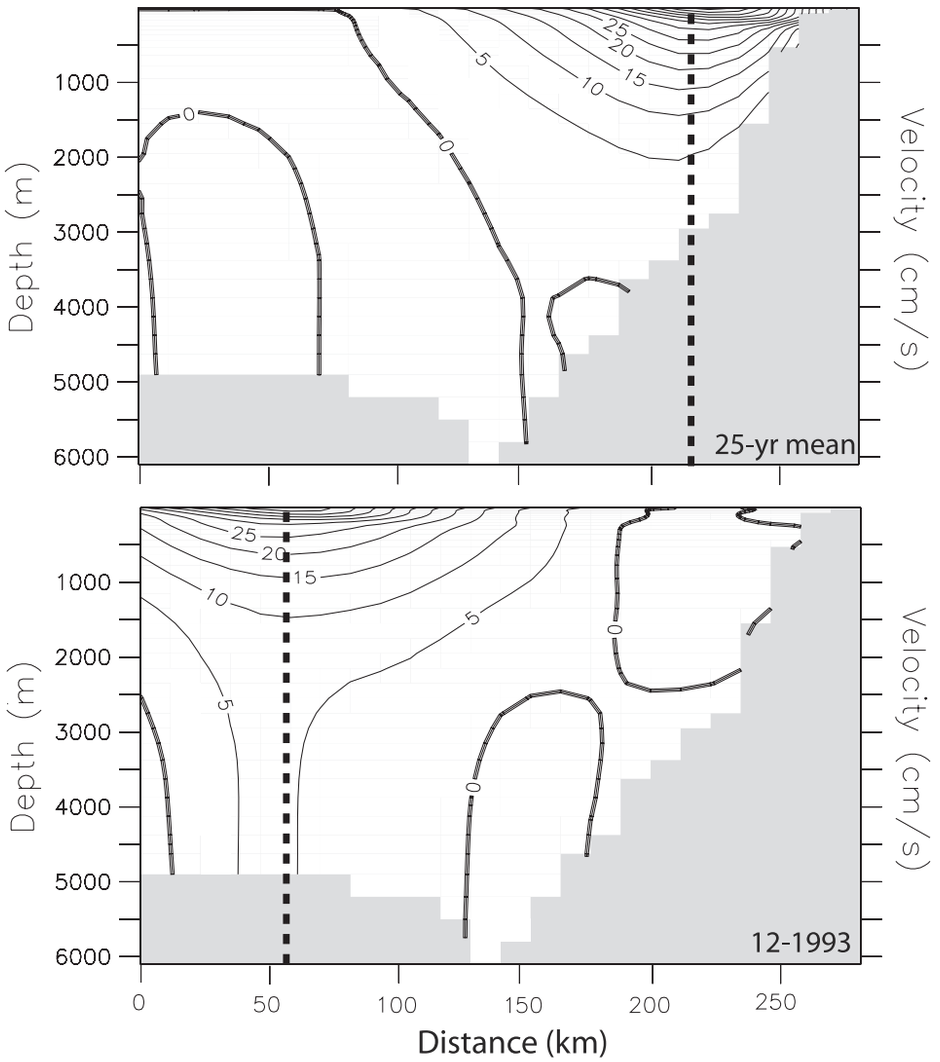

Figure 3. Vertical sections of the along-shore velocity during 1979–2003 mean (upper) and December 1993 (lower) along a line just east and south of Amukta Pass (~173.5°W) in the Alaskan Stream. The dashed lines indicate the position of the velocity cores.

D'Asaro, 1988]. As mentioned earlier, the 9-km horizontal grid cell spacing limits the model's ability to properly represent small eddies in this region that is characterized by such a small Rossby radius of deformation. On the other hand, the model simulated several eddies (both cyclonic and anticyclonic) in the Canada Basin and was even able to represent a pair of counterrotating eddies comparable to observations by *D'Asaro* [1988] and simulations by *Chao and Shaw* [1996]. Similar to predictions by *Chao and Shaw* [1996], the upper anticyclone dissipated first, in May 1986, and the lower cyclone lasted until May 1987.

5. SUMMARY AND CONCLUSIONS

Significant improvements in model skill are realized through a doubling of resolution, from 18 to 9 km. Increasingly realistic bathymetry due to higher resolution both in the horizontal and vertical direction, improves the simulation of topographically steered flows, which in the case of the Barents Sea and other coastal areas can change the representation of ocean circulation as well as regional distribution and transformation of water masses. As a result, the long-term circulation patterns in the Barents Sea agree

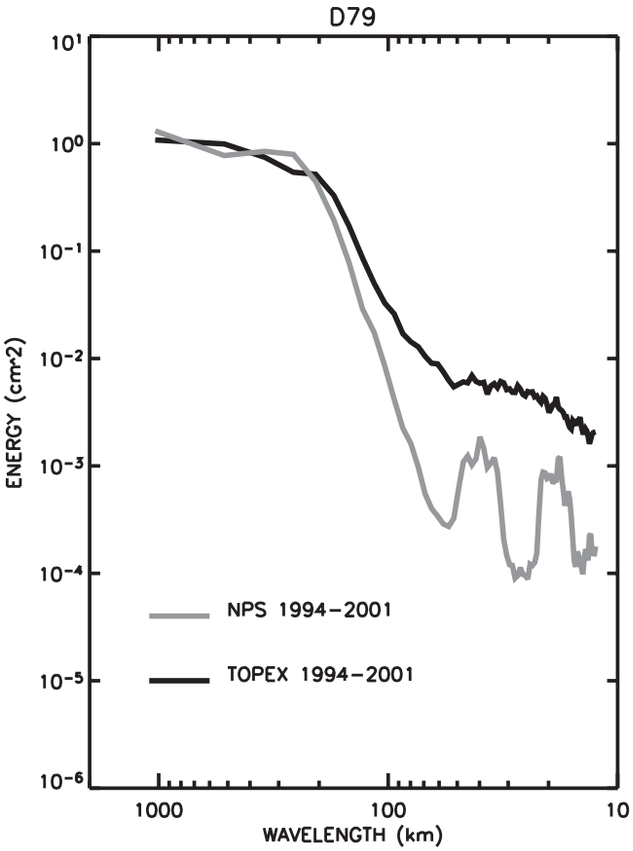

Figure 4. Eight-year mean (1994–2001) power spectra for model (gray line) and TOPEX altimeter (black line) sea surface height anomalies along TOPEX orbital ground track D79 (located along the shelf break region of the central Bering Sea).

well with published maps [*Maslowski et al*., 2004; *Ozhigin et al*., 2000]. The Atlantic Water flow through the Barents Sea, from the merging of portions of the North Cape Current and the Norwegian Coastal Current south of the Central Bank to the St. Anna Trough outflow, is more realistically defined. Calculations of EKE indicate a response to seasonal variability as well as areas of increased activity apparently associated with bathymetric features. Reducing the model grid spacing, from 18 to 9 km, has resulted in an increase in EKE by a factor of 5 in this region. It is expected that further increases in resolution will increase model EKE levels in the Barents Sea. Five numerical simulations using a closed basin quasi-geostrophic ocean model, varying only in horizontal resolution (from 25 to 1.56 km) and viscosity coefficients, and therefore Reynolds number (*Re*), indicated a continual increase in EKE with increased resolution [*Seigel et al*., 2001]. *Seigel et al*. [2001] also found that the rate of increase slows somewhat at the highest *Re*, indicating the possibility of a regime where eddy variability becomes insensitive to further increases in *Re*.

Boundary currents become narrower and stronger at 9-km resolution and the appearance of opposing boundary currents demonstrates a significant increase in horizontal and vertical shear. The representation of circulation within and around the model Labrador Sea is significantly improved. Better boundary current representation results in improvements in water mass transport around the perimeter of the Arctic Ocean as well as outflow through the Norwegian and Labrador Seas.

Comparison of the distribution of 0- to 45-m eddy kinetic energy in the Nordic/Labrador Seas between the two models shows dramatic differences (Plates 4 and 5). When viewed as an aggregate, the concentration of increased EKE in the 9-km model appears to define the path of the North Atlantic Current passing south of Iceland, and the Norwegian Atlantic Current as it travels north, along the west coast of Norway (Plate 5b). Indication of such a pathway is absent in the distribution of 18-km model EKE (Plate 5a). Based on EKE statistics computed for the regional daily snapshots (Table 2), there is an order-of-magnitude difference in magnitude between the two models. This increase in eddy kinetic energy between the 18-km model and the 9-km model has resulted in simulated values matching observed values in the southern Labrador Sea. However, 8–10° to the north, modeled values are about 20–30% lower than the observed. A definitive judgment on model skill in representing EKE in this region is difficult to make due to the differences in the atmospheric forcing between that used in the model and actual conditions. Another factor may be model resolution being just at the threshold of capturing features of a size on the order of the internal Rossby radius of deformation in the southern Labrador Sea and too coarse farther north.

Similarly in the Gulf of Alaska, EKE distribution from the 9-km model compares well, both in magnitude and spatial distribution, with estimates from observations. Model and altimeter estimates of EKE in the sub-Arctic Pacific both show high values associated with the Alaskan Stream and low values in the western Gulf of Alaska and deep Bering Sea. The model EKE values are less than the altimeter EKE values along the shelf break in the central Bering Sea. Spectral analyses of model and altimeter-measured sea surface topography suggest that the 9-km grid is not sufficiently fine to fully represent eddy energy levels at wavelengths shorter than 100–150 km.

Eddies are commonly simulated in the central Arctic Ocean in the 9-km model in similar regions as reported from observations. However, their typical size (i.e., diameter) ranges from 80 to 150 km compared to the 10- to 20-km range of observed eddies [e.g., *D'Asaro,* 1988]. We

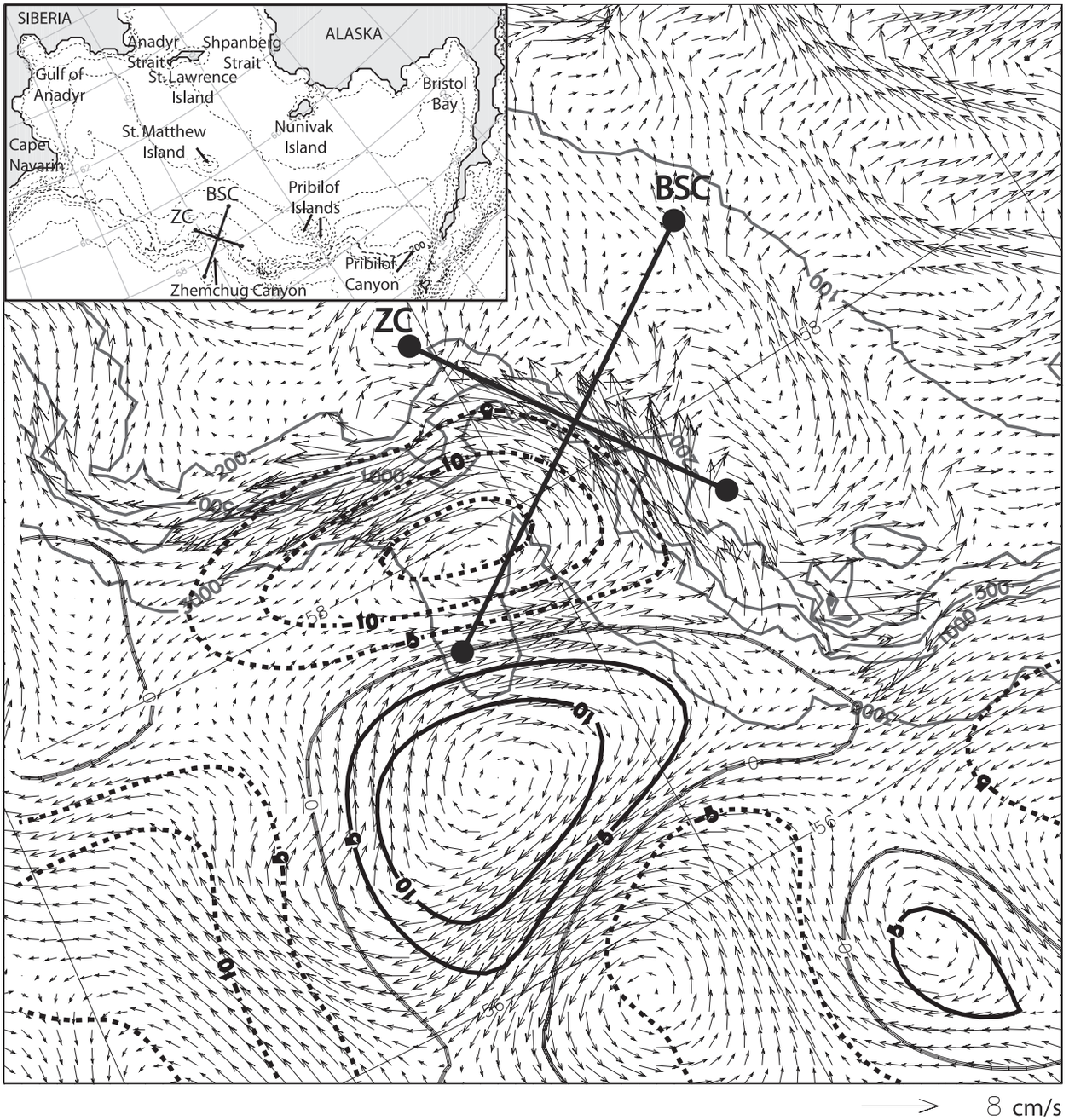

Figure 5. Velocity vectors (cm/s) and sea surface height anomaly contours (cm) during November 1993 in the vicinity of Zhemchug Canyon. Straight black lines indicate the positions of two cross sections (ZC, Zhemchug Canyon; BSC, Bering Slope Current). Solid gray lines represent bathymetry (m). Inset shows the geographic location.

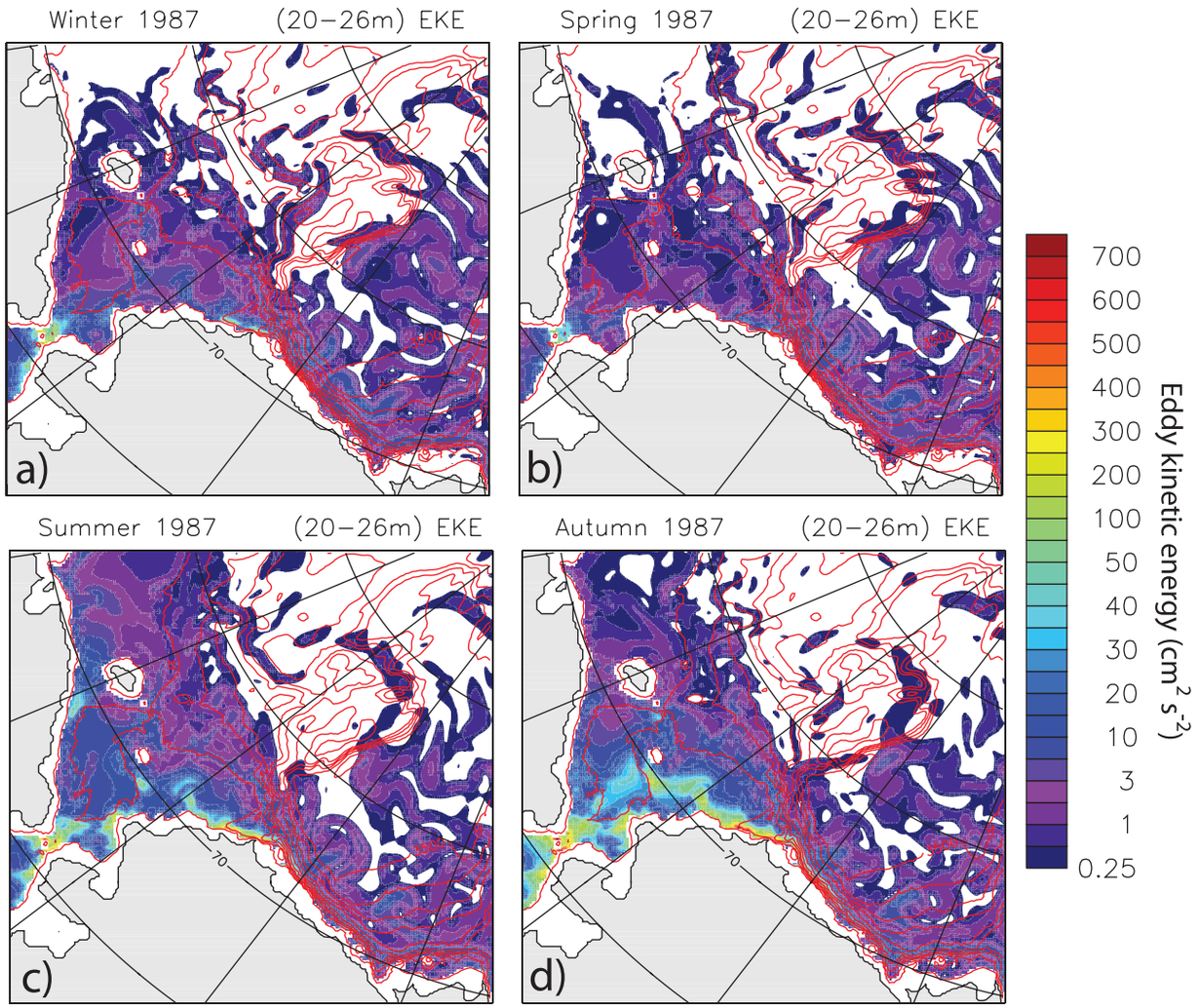

Plate 8. Eddy kinetic energy during 1987 at a depth of 20–26 m from the 9-km model for (a) winter (J-F-M), (b) spring (A-M-J), (c) summer (J-A-S), and autumn (O-N-D). Red lines indicate bathymetry.

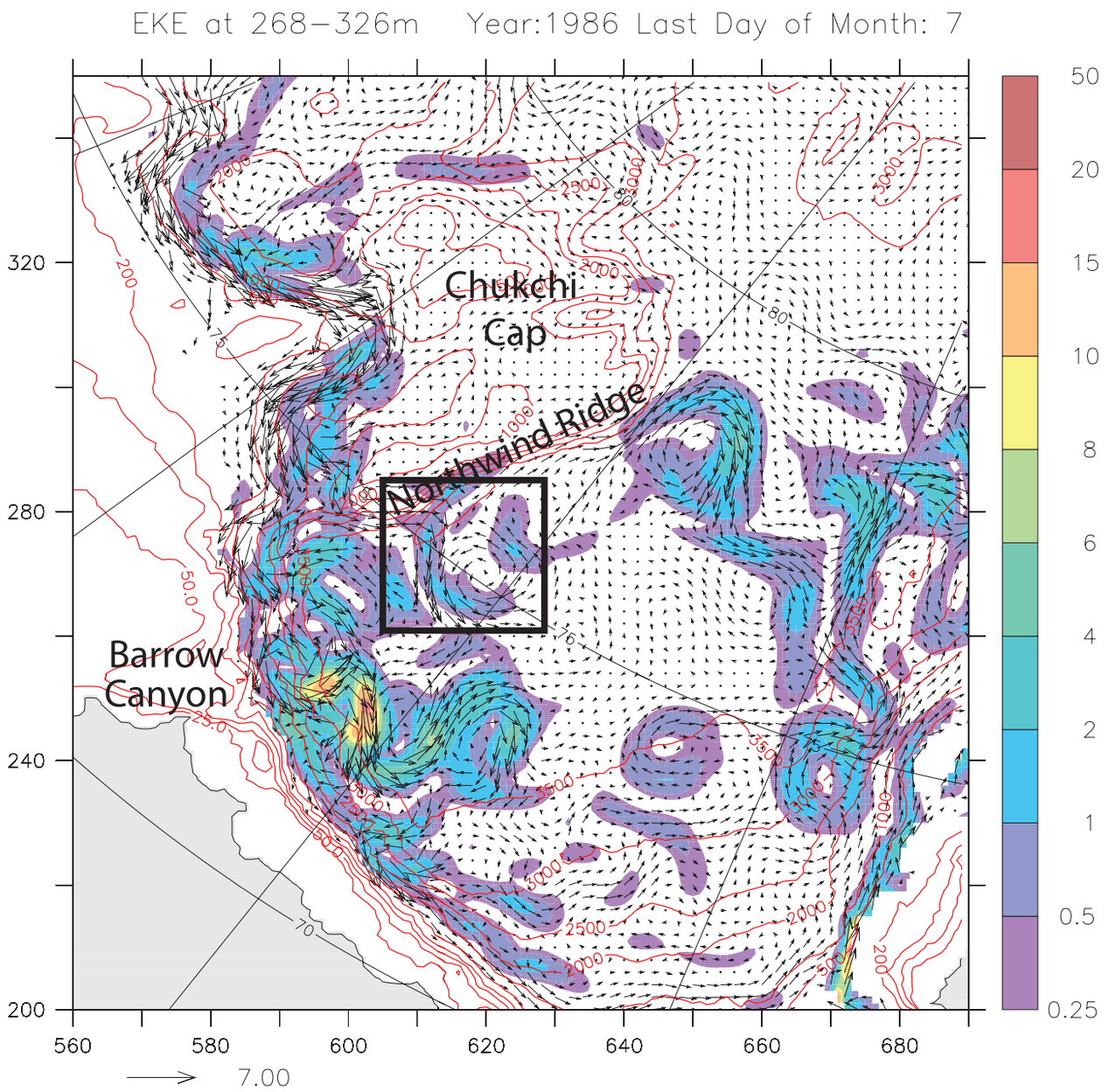

Plate 9. Modeled eddy kinetic energy (cm^2/s^2; color shading) and velocity (cm/s; vectors) in the Western Arctic from the 9-km model on July 31, 1986, at a depth of 268–326 m. Red lines indicate bathymetry. The black box indicates the region of interest for Plate 10.

Plate 10. Modeled eddy kinetic energy (cm^2/s^2; color shading) and velocity (cm/s; vectors) at (a, d) 42–53 m, (b, e) 99–122 m, and (c, f) 326–395 m from the 9-km model on November 30, 1985 (left) and May 31, 1986 (right). The black line shows the location of a vertical cross section shown in Plate 11.

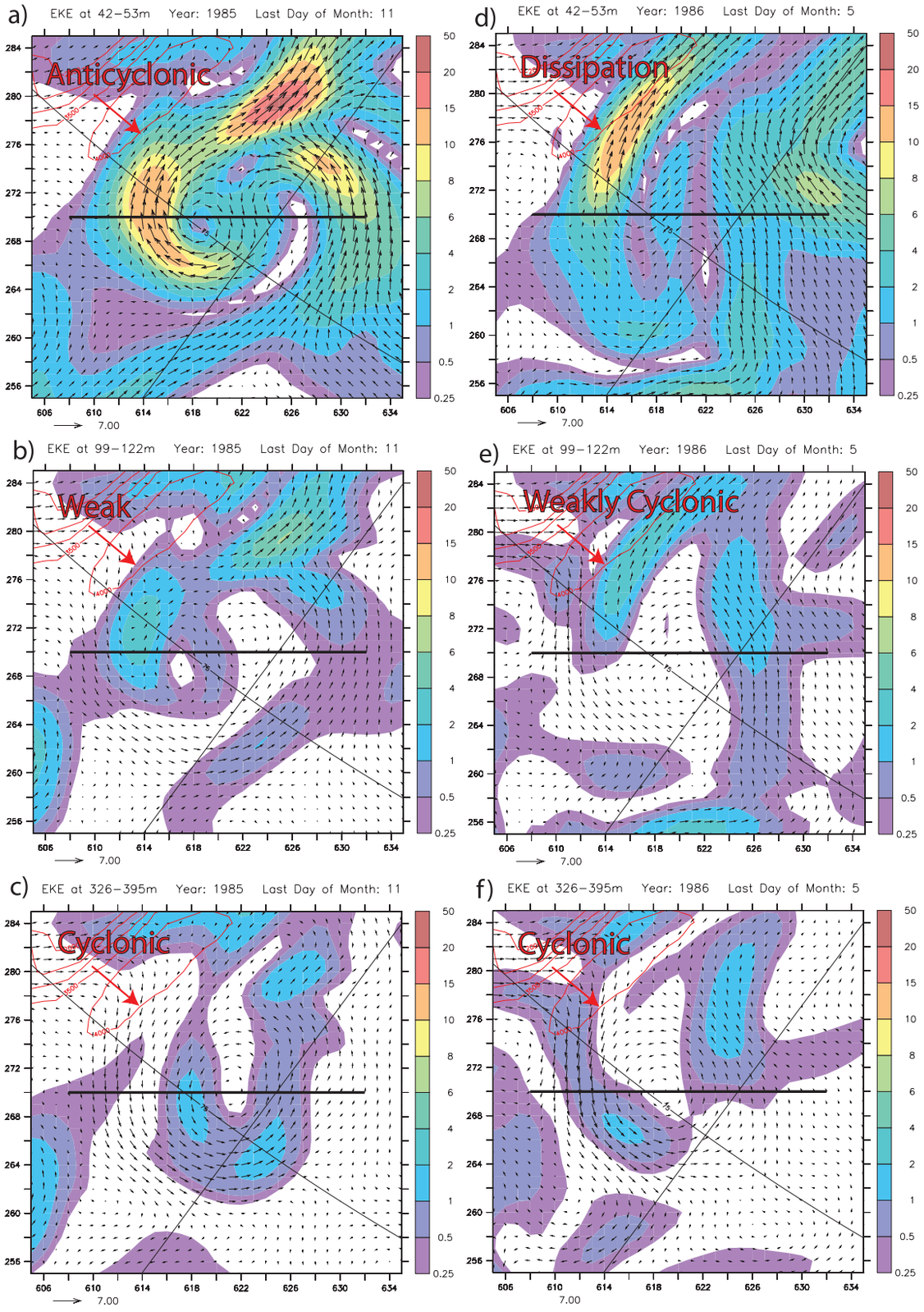
a) EKE at 42–53m Year: 1985 Last Day of Month: 11
Anticyclonic
d) EKE at 42–53m Year: 1986 Last Day of Month: 5
Dissipation
b) EKE at 99–122m Year: 1985 Last Day of Month: 11
Weak
e) EKE at 99–122m Year: 1986 Last Day of Month: 5
Weakly Cyclonic
c) EKE at 326–395m Year: 1985 Last Day of Month: 11
Cyclonic
f) EKE at 326–395m Year: 1986 Last Day of Month: 5
Cyclonic
284
280
276
272
268
264
260
256
606
610
614
618
622
626
630
634
7.00
50
20
15
10
8
6
4
2
1
0.5
0.25

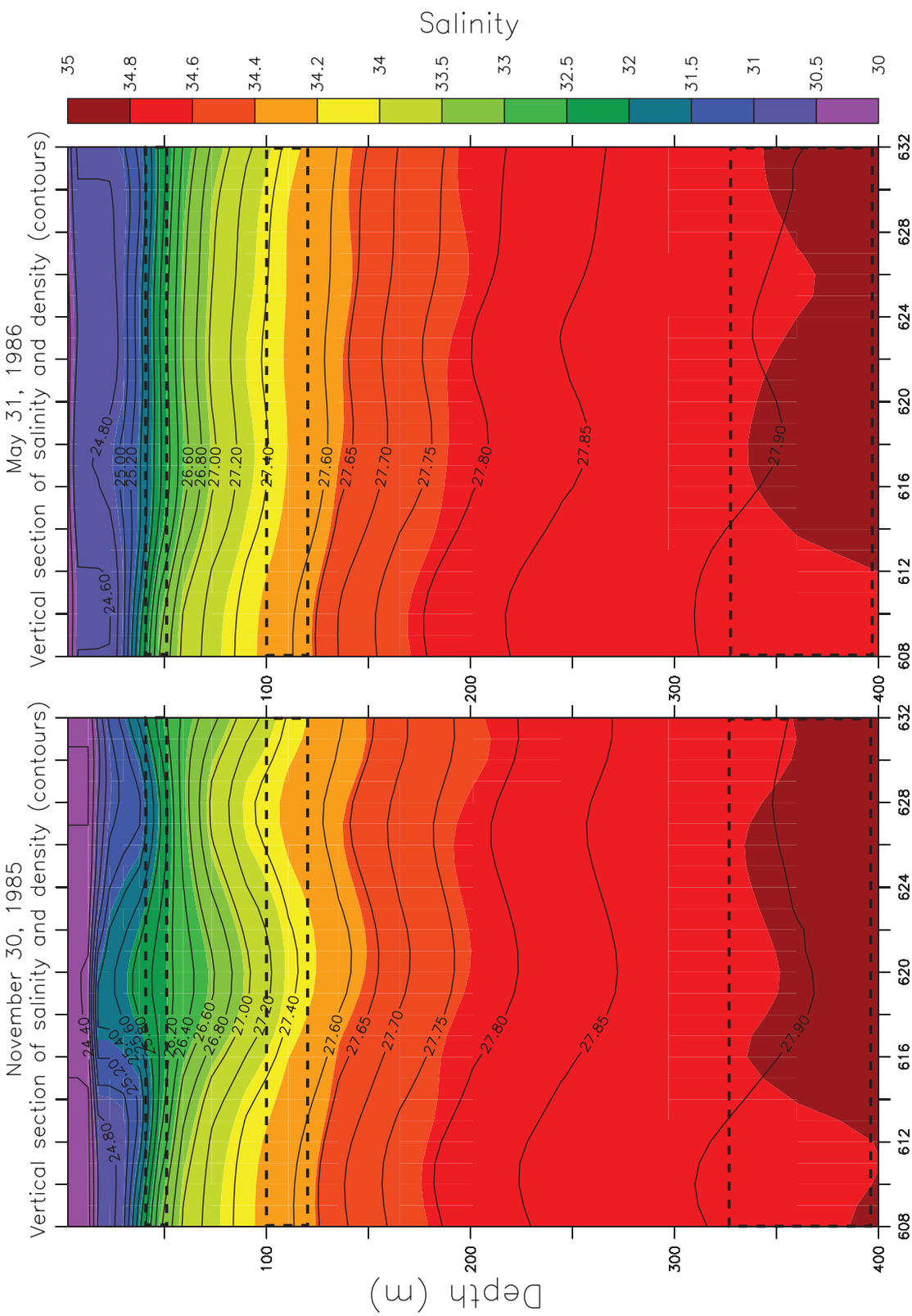

Plate 11. Modeled vertical section of salinity (color shading) and σ_θ (contours) through two counterrotating eddies from the 9-km model on November 30, 1985 (left) and May 31, 1986 (right). The black dashed boxes correspond to the three depth levels shown in Plate 10. The section location is shown in Plate 10.

hypothesize that given the limiting resolution of 9 km the model attempts to represent integrated energy of multiple smaller eddies averaged over a larger area of a modeled eddy. It is clear that significant increases in model resolution beyond 9 km are necessary to fully resolve eddies in the central Arctic. In addition, more observational data are needed to allow verification of modeled EKE distribution over larger areas.

Presented regional analyses imply that spatial resolution on the order of a few kilometers is needed to fully represent eddy energetics, in the Arctic Ocean. In addition, validation of other model results against observations (not shown) indicate that a similar horizontal resolution is required to properly represent buoyancy-driven narrow coastal currents (e.g., Alaska Coastal Current or Norwegian Coastal Current; *Maslowski and Walczowski* [2002]), small-scale bathymetry (e.g., Barrow Canyon), and land futures (e.g., passages through the CAA). Finally, more realistic and higher temporal and spatial resolution atmospheric forcing is needed for eddy-resolving ocean simulation. All these features might play a critical role in the large scale ocean dynamics as well as affect sea ice cover variability and freshwater advection and export into the North Atlantic.

Acknowledgments. Funding for the development and integration of the 18- and 9-km coupled ice-ocean models was provided by the Arctic System Science Program of the National Science Foundation, the Climate Change Prediction Program of the Department of Energy, and the Office of Naval Research. A portion of this work was toward partial completion of the requirements for a Ph.D. in physical oceanography (D.M.). Computer resources were provided by the Arctic Region Supercomputing Center (ARSC), Fairbanks, Alaska, through the Department of Defense High Performance Computer Modernization Program (DOD/HPCMP). Finally, we would like to thank the two anonymous reviewers for their comments, which helped improve the manuscript.

REFERENCES

Aagaard, K. (1989), A synthesis of the Arctic Ocean circulation, *Rapp P.-V. Reun. Cons. Int. Explor. Mer.*, *188*, pp. 11–22.

Broecker, W. S. (1991), The great ocean conveyor, *Oceanography*, *4*(2), 79–89.

Chao, S. Y., and P. T. Shaw (1996), Initialization, asymmetry, and spindown of Arctic eddies, *J. Phys. Oceanogr., 26*, 2076–2092.

Clement, J. L., W. Maslowski, L. Cooper, J. Grebmeier, and W. Walczowski (2005). Ocean circulation and exchanges through the northern Bering Sea—1979–2001 model results, *Deep-Sea Res. II*, *52*, 3509–3540, doi: 10.1016/j.dsr2.2005.09.010.

Clement Kinney, J., W. Maslowski, and S. Okkonen (2008), On the processes controlling shelf-basin exchange and outer shelf dynamics in the Bering Sea, *Deep-Sea Res. II*, in press.

Crawford, W. R., J. Y. Cherniawsky, and M. G. G. Foremann (2000), Multi-year meanders and eddies in the Alaskan Stream as observed by TOPEX/Poseidon altimeter, *Geophys. Res. Lett., 27*(7), 1025–1028.

Cuny, J., P. B. Rhines, P. P. Niiler, and S. Bacon (2002), Labrador Sea boundary currents and the fate of the Irminger sea water, *J. Phys. Oceanogr.*, *32*, 627–647.

D'Asaro, E. A. (1988), Observations of small eddies in the Beaufort Sea, *J. Geophys. Res.*, *93* (C6), 6669–6684.

Dickson, R. R., J. Meincke, S.-A. Malmberg, and A. J. Lee (1988), The "Great Salinity Anomaly" in the northern North Atlantic 1968–1982, *Progr. Oceanogr.*, *20*, 103–151.

Dickson, R. R., J. Lazier, J. Meincke, P. Rhines, and J. Swift (1996), Long-term coordinated changes in the convective activity of the North Atlantic, *Progr. Oceanogr.*, *38*, 241–295.

Gent, P. R., J. Willebrand, T. McDougall, and J. C. McWilliams (1995), Parameterizing eddy-induced tracer transports in ocean circulation models, *J. Phys. Oceanogr.*, *25*, 463–474.

Jakobsson, M., N. Z. Cherkis, J. Woodward, R. Macnab, and B. Coakley (2000), New grid of Arctic bathymetry aids scientists and mapmakers, *Eos Trans. AGU*, *81*(9), 89.

Ladd, C. A., C. W. Mordy, N. B. Kachel, and P. J. Stabeno (2007), Northern Gulf of Alaska eddies and associated anomalies, *Deep-Sea Res. I, 54*, 487–509.

Manley, T. O., and K. Hunkins (1985), Mesoscale eddies of the Arctic Ocean, *J. Geophys. Res., 90*(C3), 4911–4930.

Marble, D. C. (2001), Simulated annual and seasonal Arctic Ocean and sea-ice variability from a high resolution coupled ice-ocean model," Ph.D. dissertation, Naval Postgraduate School, September 2001.

Maslowski, W., and W. Walczowski (2002), On the circulation of the Baltic Sea and its connection to the Pan-Arctic region—A large scale and high-resolution modeling approach, *Boreal Environ. Res.*, *7*, 319–325.

Maslowski, W., B. Newton, P. Schlosser, A. J. Semtner, and D. Martinson (2000), Modeling recent climate variability in the Arctic Ocean, *Geophys. Res. Lett., 27*(22), 3743–3746.

Maslowski, W., D. C. Marble, W. Walczowski, and A. J. Semtner (2001), On large-scale shifts in the Arctic Ocean and Sea Ice Conditions during 1979–98, *Ann. Glaciol.*, *33*, 319–325.

Maslowski, W., D. Marble, W. Walczowski, U. Schauer, J. L. Clement, and A. J. Semtner (2004), On climatological mass, heat, and salt transports through the Barents Sea and Fram Strait from a pan-Arctic coupled ice-ocean model simulation, *J. Geophys. Res., 109*, C03032, doi:10.1029/2001JC001039.

Maslowski, W., R. Roman, and J. Clement Kinney (2008), Effects of mesoscale eddies on the flow of the Alaskan Stream, *J. Geophys. Res*., in press.

Mizobata, K., J. Wang, and S. Saitoh (2006), Eddy-induced cross-slope exchange maintaining summer high productivity of the Bering Sea shelf break, *J. Geophys. Res*., *111*, C10017, doi:10.1029/2005JC003335.

Nazarenko, L., T. Sou, M. Eby, and G. Holloway (1997), The Arctic ocean-ice system studied by contamination modelling, *Ann. Glaciol.*, *25*, 17–21.

Nazarenko, L., G. Holloway, and N. Tausnev (1998), Dynamics of transport of "Atlantic signature" in the Arctic Ocean, *J. Geophys. Res.*, *103*(C13), 31,003–31,015.

Okkonen, S. R. (1992), The shedding of an anticyclonic eddy from the Alaskan Stream as observed by the Geosat altimeter, *Geophys. Res. Lett., 19*(24), 2397–2400.

Okkonen, S. R. (1993), Observations of topographic planetary waves in the Bering Slope Current using Geosat altimeter, *J. Geophys. Res. 98*(C12) 22,603–22,613.

Ozhigin, V. K., A. G. Trofimov, and V. A. Ivshin (2000), The Eastern Basin Water and currents in the Barents Sea, in *ICES Annual Science Conference 2000*.

Pfirman, S. L., D. Bauch, and T. Gammelsrod (1994), The Northern Barents Sea: Water Mass Distribution and Modification, in *The Polar Oceans and Their Role in Shaping the Global Environment: The Nansen Centennial Volume*, *Geophys. Monogr. Ser.,* vol. 85, edited by O. M. Johannesen, R. D. Muench, and J. E. Overland, pp. 77–94, AGU, Washington, D. C.

Pickart, R. S., T. J. Weingartner, L. J. Pratt, S. Zimmermann, D. J. Torres (2005), Flow of winter-transformed Pacific water into the Western Arctic, *Deep-Sea Res., 52*, 3175–3198, doi: 10.1016/j.dsr2.2005.10.009.

Plueddemann, A. J., R. Krishfield, T. Takizawa, K. Hatakeyama, and S. Honjo (1998), Upper ocean velocities in the Beaufort Gyre, *Geophys. Res. Lett., 25*(2), 183–186.

Reed, R. K., and P. J. Stabeno (1999), A recent full-depth survey of the Alaskan Stream, *J. Oceanogr., 55*, 79–85.

Rudels, B. (1987), On the mass balance of the Polar Ocean, with special emphasis on the Fram Strait, *Norsk Polarinst. Skr.*, *188*, 53 pp.

Rudels, B., E. P. Jones, L. G. Anderson, and G. Kattner (1994), On the intermediate depth waters of the Arctic Ocean, in *The Polar Oceans and Their Role in Shaping the Global Environment: The Nansen Centennial Volume*, *Geophys. Monogr. Ser.,* vol. 85, edited by O. M. Johannesen, R. D. Muench, and J. E. Overland, pp. 33–46, AGU, Washington, D. C.

Schumacher, J. D., and P. J. Stabeno (1994), Ubiquitous eddies of the Eastern Bering Sea and their coincidence with concentrations of larval pollock, *Fish. Oceanogr.*, *3*, 182–190.

Seigel, A., J. B. Weiss, J. Toomre, J. C. McWilliams, P. S. Berloff, and I. Yavneh (2001), Eddies and vortices in ocean basin dynamics, *Geophys. Res. Lett., 28*(16), 3183–3186.

Semtner, A. J., Jr., and R. M. Chervin (1992), Ocean general circulation from a global eddy-resolving model, *J. Geophys. Res.*, *97*(C4), 5493–5550.

Skyllingstad, E. D., D. W. Denbo, and J. Downing (1991), Convection in the Labrador Sea: Community Modeling Effort (CME) results, in *Deep Convection and Deep Water Formation in the Oceans*, edited by P. C. Chu and J. C. Gascard, Elsevier, New York, NY.

Stabeno, P., and R. Reed (1994), Circulation in the Bering Sea Basin Observed by Satellite-Tracked Drifters: 1986–1993. *J. Phys. Oceanogr.*, *24*, 848–854.

Stevens, D. P., and P. D. Kilworth (1992), The distribution of kinetic energy on the Southern Ocean: A comparison between observations and an eddy resolving general circulation model, *Philos. Trans. Biol. Sci*., *338*(1285), Antarctica and Environmental Change, pp. 251–257.

Visbeck, M., J. Fischer, and F. Schott (1995), Preconditioning the Greenland Sea for deep convection: Ice formation and ice drift, *J. Geophys. Res.*, *100*(C9), 18,489–18,502.

White, M. A., and K. J. Heywood (1995), Seasonal and interannual changes in the North Atlantic subpolar gyre from Geosat and TOPEX/POSEIDON altimetry, *J. Geophys. Res.*, *100*(C12), 24,931–24,941.

W. Maslowski, Department of Oceanography, Naval Postgraduate School, Monterey, California, USA.

J. Clement Kinney, Department of Oceanography, Naval Postgraduate School, Monterey, California, USA.

D. C. Marble, Office of Naval Research, Code 322, Arlington, Virginia, USA.

J. Jakacki, Institute of Oceanography, Polish Academy of Sciences, Sopot, Poland.